Research Article

Journal of Environmental Nanotechnology

Green-synthesized Zinc–copper–cobalt Oxide Nanoparticles: Structural, Morphological, Optical and Electrochemical Characterization for Photocatalytic and Supercapacitor Applications

Shruti A. Gomkale[1], G. Subramaniam[2*], S. Mayakannan[3,4], G. Chandrasekaran[5], A. V. S. Ram Prasad[6] and R. Suresh[7]

[1]Department of Applied Chemistry, Yeshwantrao Chavan College of Engineering, Nagpur, MH, India
[2]Department of Electrical and Electronics Engineering, M. Kumarasamy College of Engineering, Karur, TN, India
[3]Department of Mechanical Engineering, Saveetha School of Engineering, Saveetha Institute of Medical and Technical Sciences, SIMATS, Chennai, TN, India
[4]Department of Mechanical Engineering, Rathinam Technical Campus, Coimbatore, TN, India
[5]Department of Mechanical Engineering, Lord Jegannath College of Engineering and Technology, Nagercoil, TN, India
[6]Department of Mechanical Engineering, Koneru Lakshmaiah Education Foundation, Guntur, AP, India
[7]Department of Mechanical Engineering, Vel Tech High Tech Dr. Rangarajan Dr. Sakunthala Engineering College, Tiruvallur, TN, India
Received: 04.07.2026 Accepted: 01.08.2026 Published: 30.09.2026
*subramaniamgphd26@gmail.com

ABSTRACT

This study presents green synthesis of Zinc-Copper-Cobalt Oxide (ZCCO) using tulsi leaf extract as natural reducing agent. Nanoparticles were characterized to evaluate morphological, optical, structural, photocatalytic, and electrochemical characteristics. Powder X-ray diffraction (PXRD) analysis confirmed formation of crystalline mixed-metal oxide phase, while microscopic investigations revealed uniformly distributed nanosized particles with a distinct surface morphology. UV–Visible diffuse reflectance studies demonstrated efficient light absorption characteristics, indicating the suitability of the material for photocatalytic applications. Photocatalytic activity of nanoparticles was examined by degradation of organic dye pollutants under ultraviolet irradiation. The synthesized material exhibited remarkable dye degradation efficiency, demonstrating its potential for wastewater treatment applications. Electrochemical properties were further analysed by galvanostatic charge–discharge measurements, cyclic voltammetry, and electrochemical spectroscopy at alkaline electrolyte. The ZCCO nanoparticles displayed enhanced charge-transfer behavior, strong redox activity, and promising energy-storage performance. These findings suggest that, tulsi-mediated zinc-copper-cobalt oxide nanoparticles can serve as an effective multifunctional material for environmental remediation and electrochemical energy-storage technologies, thereby promoting sustainability. Furthermore, galvanostatic charge–discharge analysis confirmed good capacitive characteristics and excellent electrochemical stability, highlighting their suitability for supercapacitor and advanced energy-storage applications.

Keywords: Absorption; Photocatalytic activity; UV-irradiation; Waste water treatment; Cyclic voltammetry.

1. INTRODUCTION

Green synthesis approaches have gained increasing attention for developing sustainable nanomaterials by minimizing hazardous chemical usage. Tulsi (*Ocimum tenuiflorum*) leaf extract, rich in bioactive phytochemicals, acts as capping agent and natural reducing for eco-friendly synthesis of Zinc-Copper-Cobalt oxide Nanoparticles (ZCCO) nanoparticles. Transition metal oxide nanocomposites, including cobalt, manganese, iron, titanium, vanadium, copper, and zinc-based systems, exhibit enhanced conductivity and electrochemical activity, significantly improving supercapacitor performance and energy storage capability for next-generation applications (Nandagudi *et al.* 2022). Hydrothermally synthesized Fe_2O_3 nanorods have been reported as efficient electrode material for supercapacitor applications. The material exhibits high crystallinity, excellent capacitance performance, and good cyclic stability, making it suitable for advanced energy storage devices (Khawale *et al.* 2024). ZnO/Co_3O_4 nanocomposites synthesized *via* co-precipitation exhibited good electrochemical activity and sensing performance, demonstrating the potential of mixed metal oxides for electrochemical applications (Arpitha *et al.* 2023). Mn-doped zinc oxide/reduced graphene oxide exhibited improved electrochemical and photoelectrochemical efficiency. The optimized composition demonstrated excellent charge storage capability and cycling stability, making it suitable for supercapacitor uses (Ansari *et al.* 2025).

The rGO–ZnO–Elwendia persica seed composite showed specific capacitance of 535 F g^{-1} at 1

A g^{-1} with 90% capacitance retention after 3000 cycles. Its porous structure and low electrical resistance contributed to excellent supercapacitor performance (Salamon *et al.* 2025). Conductive hybrid systems such as ZCO@PANI and mechanochemically synthesized Cu-HHTP have also shown excellent electrical and charge-storage characteristics for next-generation supercapacitors (Pandey *et al.* 2026; Marchetti *et al.* 2026).

Tulsi extract contains bioactive phytochemicals as natural reducing and stabilizing agents for the green synthesis of metallic nanoparticles, which have demonstrated promising catalytic and photocatalytic properties, showing potential of tulsi-mediated routes for sustainable nanotechnology (Singh, 2022). Tulsi-mediated iron nanoparticles exhibited superior photocatalytic performance, achieving 83% degradation of gentian violet dye under visible-light irradiation. Enhanced activity was attributed to band-gap reduction, high adsorption capacity, and reactive oxygen species generation, highlighting their potential for wastewater treatment applications (Kumari *et al.* 2023). Likewise, tulsi-mediated ZnO/GCN nanohybrids and Mg-doped manganese ferrite nanoparticles exhibited enhanced photocatalytic activity and improved functional properties arising from synergistic interactions, reduced band- gaps, and favorable nanostructures (Panchal *et al.* 2025; Adarshgowda *et al.* 2024). Scanning Electron Microscopy (SEM) analysis revealed that the green-synthesized NiO nanoparticles possessed a homogeneous spherical morphology with average particle size of 18.3 nm, indicating successful phytochemical-assisted formation and uniform particle distribution (Revathi *et al.* 2026).

Zn-doped nickel molybdate nanoparticles exhibited enhanced photocatalytic activity and excellent pseudocapacitive behavior because of high surface area and reduced band-gap. The optimized material reached high capacitance of 826 F/g and improved dye degradation efficiency, highlighting their potential for environmental remediation and energy storage applications (Soundarraj *et al.* 2026). β-$Cu_2V_2O_7$ nanoparticles exhibited excellent photocatalytic performance, achieving 94% dye degradation under visible light irradiation. The material also delivered specific capacitance of 310 F/g and 96.48% retention after 2500 cycles, showing potential for energy storage uses (Pooja *et al.* 2025). Co-doped zinc manganite spinels exhibited enhanced photocatalytic and electrochemical performance compared to the undoped material. The optimized composition achieved 87% dye degradation, a specific capacitance of 486 F/g, and 88% capacitance retention after 1000 cycles, demonstrating its excellent bifunctional performance and strong potential for environmental remediation and electrochemical energy storage applications (Jose *et al.* 2023). The Zn:NiO nanocomposite exhibited 84.46% photocatalytic degradation of Fast Orange (FO) red dye under UV irradiation and a band-gap of 3.34 eV. The material delivered a specific capacitance of 239.8 F/g at 1 A/g and retained 81.5% capacitance after 3000 cycles, demonstrating its suitability for supercapacitor applications (Vusenappagari and Kumar, 2025).

The $CuInO_2$@Ti_3C_2 composite exhibited high specific capacitance of 526 F/g at 1 A/g and 88% capacitance after 4000 cycles, demonstrating excellent electrochemical stability. The asymmetric device showed a power density of 2998 W $kg^{-1}$and density of 24.06 Wh kg^{-1}, highlighting its potential for supercapacitor applications (Surya *et al.* 2025). Polymer–metal complex-based electrode materials have been widely explored for supercapacitor applications due to their enhanced conductivity, stability, and charge storage capability. Co-based organometallic polymers showed high capacitance of 793 F g^{-1} along with energy density (Maskaric *et al.* 2026). CuO–ZnO/3D P, N co-doped rGO (CZ/3DNPG) nanocomposites have been reported as efficient supercapacitor electrode materials with enhanced porosity, surface area, and charge-transfer kinetics. The material delivered a high specific capacitance of 714 F g^{-1} at 1 A g^{-1} with excellent cycling stability, displaying the synergistic effect of metal oxides (Nazari *et al.* 2026). Hierarchical $CuCo_2O_4$/rGO/MnCo LDH nanocomposites have been reported to exhibit outstanding electrochemical efficiency, delivering capacitance of 1408 F g^{-1} at 1 A g^{-1}, demonstrating the effectiveness of hierarchical hybrid architectures for high-performance supercapacitor applications (Allah *et al.* 2026).

Ion-doping strategies enhance electrochemical efficiency of transition metal sulfides by improving conductivity and generating vacancy-rich structures. Co,N co-doped ZnS exhibited higher capacitance (1554 F g^{-1}) than Cu,N co-doped ZnS (1299 F g^{-1}), demonstrating effective dual-ion doping for energy storage applications (Tian *et al.* 2026). Mixed quaternary CoNiCuZn oxide electrodes demonstrated exceptional electrochemical performance with a maximum specific capacitance of 2078.33 mAh/g, while the symmetric device achieved an energy density of 14.32 Wh/kg and 94% capacitance retention after 2500 cycles, indicating strong potential for high-efficiency supercapacitor uses (Gaikwad *et al.* 2026). Green-synthesized CMA–ZCCO nanomaterials exhibited efficient photocatalytic dye degradation and promising supercapacitor performance, with enhanced electrochemical activity, good capacitance, and excellent cycling stability for environmental and energy storage applications (Viswanathan *et al.* 2026)

Conventional nanoparticle synthesis may involve chemical reagents and energy-intensive processing, raising environmental concerns. Plant-mediated synthesis provides a more sustainable route for

metal-oxide nanoparticle preparation; for example, cobalt oxide nanoparticles have been successfully synthesized using *Ziziphus oenopolia* leaf extract. (Kavica *et al.* 2024) Green synthesis techniques provide a sustainable alternative by reducing chemical consumption, lowering energy demand, and promoting environmentally responsible material production. In the present study, tulsi leaf extract was utilized as natural stabilizing and reducing agent for the eco-friendly synthesis of Zinc-copper-cobalt oxide nanoparticles. The prepared nanoparticles were characterized by PXRD, SEM, and UV–DRS techniques to investigate their phase composition, surface morphology, particle structure, and optical behavior. In addition, electrochemical activity evaluated charge-transfer characteristics and energy-storage capability of synthesized material. The photocatalytic efficiency and supercapacitive performance of ZCCO nanoparticles were further examined through galvanostatic charge–discharge, electrochemical impedance spectroscopy and cyclic voltammetry (CV) measurements.

2. EXPERIMENTAL METHODOLOGY

2.1 Materials and Methods

Chemicals required for synthesis of zinc-copper-cobalt oxide nanoparticles were obtained from Star Scientific, Erode, Tamil Nadu, India. They were used directly without further purification.

2.2 Preparation of the Leaf Extract

Fresh tulsi (*Ocimum tenuiflorum*) leaves were washed with deionized water and air-dried. To prepare leaf extract, 25 g of dried leaves were finely cut and heated in deionized water at 60 °C of 20 minutes at continuous magnetic stirring. Resulting solution was filtered by filter paper, and obtained extract was refrigerated at 4 °C for subsequent synthesis of ZCCO nanoparticles.

2.3 Green Synthesis of Zinc-copper-cobalt Oxide Nanoparticles

An aqueous precursor solution was formulated using double-distilled water and stoichiometric quantities of cobalt nitrate [$Co(NO_3)_2 \cdot 6H_2O$], zinc nitrate [$Zn(NO_3)_2 \cdot 6H_2O$], and copper nitrate [$Cu(NO_3)_2 \cdot 3H_2O$], in an appropriate molar proportion. Subsequently, 1 mL of tulsi leaf extract were introduced at solution and magnetically stirred for approximately 30 minutes to obtain uniform reaction mixture. The precursor solution was placed at furnace maintained at 500 °C, where an autocombustion reaction took place, producing zinc-copper-cobalt oxide nanoparticles along with the release of gaseous byproducts. The as-synthesized powder was subjected to calcination at 900 °C for 3 hours to enhance crystallinity, phase purity, and structural stability (Yadav *et al.* 2026).

2.3.1 Precursor Solution Preparation

Stoichiometric amounts of copper nitrate, cobalt nitrate and zinc nitrate were dissolved at double-deionized water to prepare clear and uniform precursor solution with the desired molar ratio for synthesis of ZCCO nanoparticles.

2.3.2 Green Reducing Agent

Thereafter, 1 mL of Tulsi leaf extract was added to precursor mixture. The extract contains various bioactive compounds, like phenolics, flavonoids, terpenoids, and other phytoconstituents, which act as natural reducing, chelating, and fuel agents, thereby maintaining green synthesis of ZCCO nanoparticles.

2.3.3 Mixing

Reaction mixture was continuously agitated using magnetic stirrer for 30 minutes to ensure thorough mixing, effective interaction of the metal precursors with the tulsi extract, and the formation of a homogeneous solution.

2.3.4 Combustion Reaction

Homogeneous precursor solution was transferred to furnace maintained at 500 °C, where a self-propagating combustion reaction was initiated. During this process, the metal nitrates underwent thermal decomposition with the release of gaseous byproducts, resulting in the formation of ZCCO nanoparticles.

2.3.5 Formation of Nanomaterials

The rapid autocombustion reaction produced zinc-copper-cobalt oxide nanoparticles with a lightweight and highly porous structure, which resulted from the continuous evolution of gaseous products during the combustion stage.

2.3.6 Calcination

The as-prepared ZCCO powder was subsequently heat-treated at 900 °C for 3 hours to enhance crystal growth, phase formation, and structural stability. A schematic representation of green synthesis procedure is presented in Fig. 1.

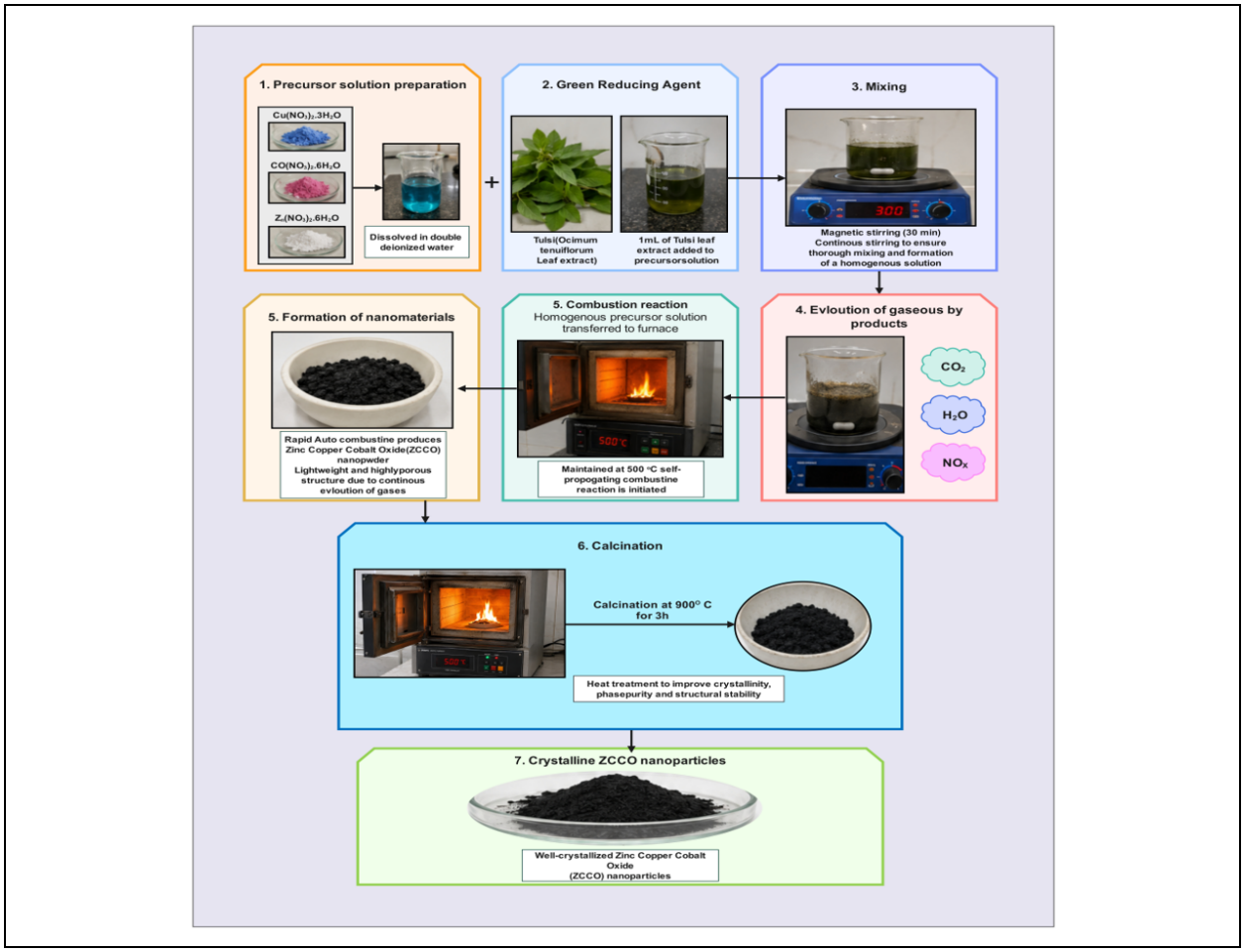

Fig. 1: Schematic illustration of the green combustion synthesis of tulsi-mediated ZCCO nanoparticles

2.4 Electrode Preparation

For the cyclic voltammetry measurements, a nickel mesh was employed as the current collector, while platinum electrodes and Ag/AgCl served counter and reference electrodes. The ZCCO nanoparticles, graphite powder (98% purity, particle size >20 µm), and PTFE binder were mixed at weight ratio of 15:70:15 to make working electrode material. The constituents were ground using agate mortar for 30 minutes until uniform and cohesive paste was obtained. The resulting paste was then coated onto a nickel mesh substrate to establish effective electrical contact among active material and current collector. Prior to electrochemical testing, the electrode was immersed at 1.0 M KOH electrolyte for 25 minutes to ensure adequate electrolyte penetration and activation. The exposed wire connections and the reverse side of the electrode were insulated using Teflon tape to prevent unwanted electrochemical interactions (Kubendhiran *et al.* 2025).

2.5 Characterization

The phase composition and crystal structure of green-synthesized ZCCO nanoparticles were analyzed by Bruker X-ray diffractometer. Optical absorption characteristics in UV–visible region were examined by Shimadzu UV-2600 spectrophotometer. Surface morphology and elemental composition were evaluated by Gemini, Zeiss scanning electron microscope equipped by EDX spectroscopy detector (Gunasekaran *et al.* 2025). Electrochemical properties were analysed by CHI608E workstation in 3-electrode configuration. EIS and CV measurements were conducted in 1 M KOH electrolyte.

3. RESULTS AND DISCUSSION

3.1 Powder X-ray Diffraction Studies

Fig. 2 shows the PXRD pattern of tulsi-assisted ZCCO nanoparticles. Diffraction peaks at 2θ values of 18.7°, 31.3°, 36.8°, 38.6°, 44.7°, 55.5°, 59.3°, 65.1°, and 77.2° correspond to the crystallographic planes of (111), (220), (311), (222), (400), (422), (511), (440), and (533). These reflections indicate formation of a crystalline spinel-type mixed-metal oxide structure.

The diffraction pattern verified the crystalline nature of ZCCO nanoparticles. Based on the peak

broadening analysis using Debye–Scherrer formula, mean crystallite size was estimated to be 19.8 nm.

$$D = \frac{K\lambda}{\beta \cos\theta} \quad \ldots (1)$$

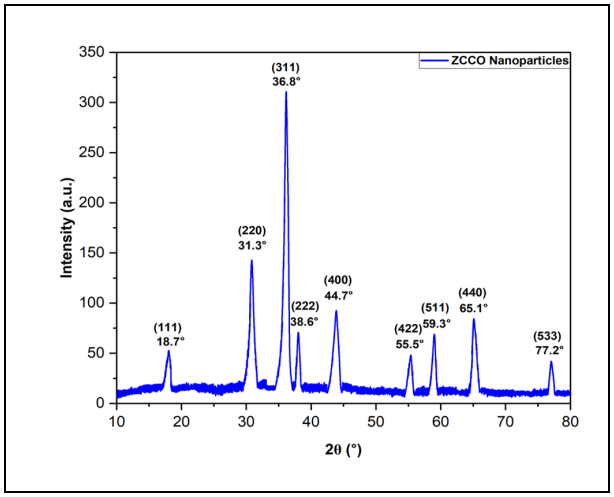

Fig. 2: PXRD pattern of ZCCO nanoparticles

Table 1. Calculated values of ZCCO nanoparticles

2θ	FWHM	Crystallite Size	d-Spacing	Miller Indices
17.5	0.525	21.00	2.77	100
23.5	0.478	18.74	2.51	001
32.1	0.391	20.78	2.37	101
34.0	0.587	16.93	1.81	020
37.1	0.500	18.81	1.52	121
41.5	0.717	17.65	1.35	111
42.8	0.749	16.30	1.26	120
50.7	0.614	18.5	1.94	201
53.9	0.712	19.1	1.85	220
62.2	0.524	20.1	2.01	130
64.2	0.641	19.5	1.74	202
67.3	0.631	21.2	1.86	113

In the Debye–Scherrer equation, K represents shape factor, λ shows wavelength of incident X-ray radiation, and β corresponds to full width at half maximum (FWHM) of diffraction peak. The structural parameters of synthesized ZCCO nanoparticles were subsequently determined using the following crystallographic relationship.

$$\frac{1}{d^2} = \frac{4}{3}\left[\frac{h^2 + hk + l^2}{a^2}\right] + \frac{l^2}{c^2} \quad \ldots (2)$$

In this equation, (hkl) represents Miller indices of corresponding diffraction plane, a shows lattice parameter, and $dhkl$ denotes to interplanar spacing associated with respective crystal plane. The calculated FWHM values, d-spacings, crystallite sizes, and indexed diffraction planes of the tulsi-mediated ZCCO nanoparticles are summarized in Table 1.

The obtained d-spacing values showed only minor deviations from the standard reference data, indicating good crystallinity and successful formation of the desired ZCCO phase. According to previous studies, XRD analysis revealed the formation of a stable crystalline phase, confirming the successful incorporation of Ag ions into the host lattice. The absence of significant impurity peaks further indicates good phase purity and structural stability. Similar crystallographic behavior has been reported for Ag-containing systems in previous XRD and phase equilibrium studies (Moroz *et al.* 2024).

3.2 Studies using Scanning Electron Microscopy

Scanning electron microscopy was employed to analyse microstructural features and surface morphology of synthesized ZCCO nanoparticles. Similar well-defined ZCCO nanostructures have been reported to provide large active surface area, thereby enhancing electrochemical performance (Rahman *et al.* 2022). The SEM micrographs presented in Fig. 3 (a,b) reveal that, the tulsi-assisted ZCCO nanoparticles were agglomerated into irregular, porous secondary particles with quasi-spherical to clustered morphologies. The observed agglomeration is attributed to the high surface energy of nanoparticles generated during the combustion synthesis process. Porous architecture and interconnected particle network provide a large accessible surface area, which is beneficial for photocatalytic and electrochemical applications. The phytochemical constituents present in the tulsi extract likely acted as natural capping and stabilizing agents, regulating the growth of the primary crystallites while suppressing excessive particle coalescence. Although the average crystallite size determined from PXRD was approximately 19.8 nm, the SEM images predominantly revealed larger agglomerated secondary particles composed of these nanosized crystallites. In addition, a few localized irregular features and surface roughness were observed, which may be attributed to rapid gas evolution and thermal decomposition during the combustion process.

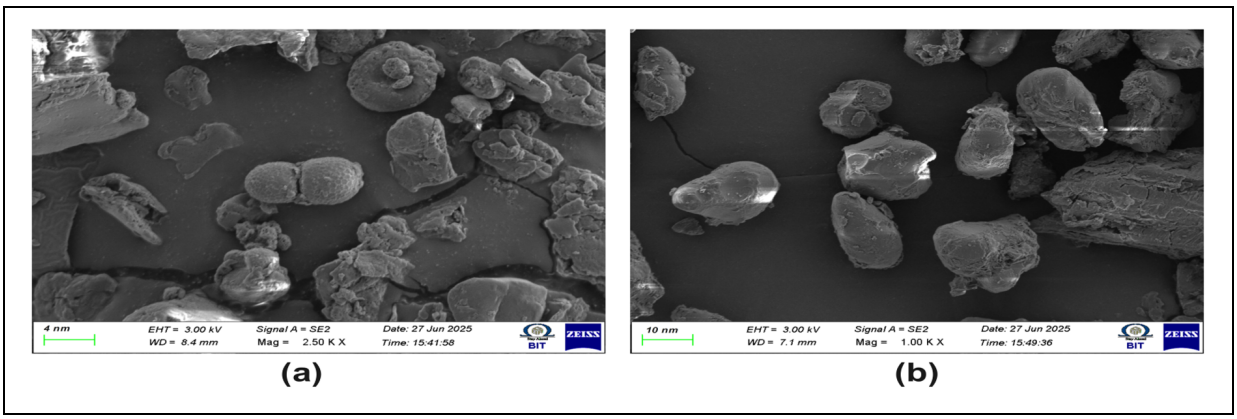

Fig. 3: SEM micrographs of ZCCO nanoparticles

3.3 UV- Diffuse Reflectance Spectroscopy Spectrum

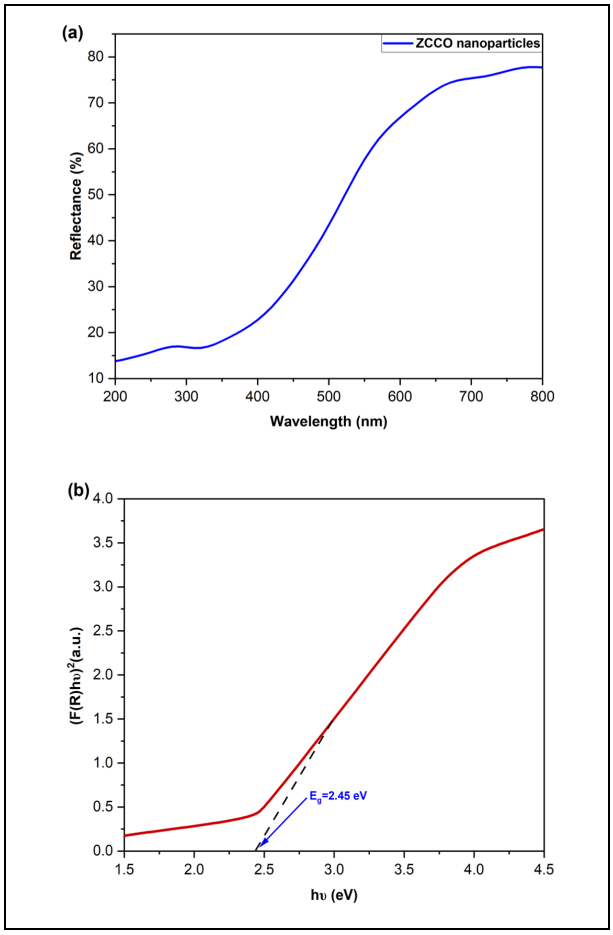

Fig. 4: (a) UV-Vis-DR spectrum and (b) Kubelka–Munk plot for optical band-gap determination of ZCCO nanoparticles

Optical properties of tulsi-mediated ZCCO nanoparticles were investigated using diffuse reflectance spectroscopy in wavelength of 200–800 nm. Diffuse Reflectance Spectroscopy (DRS) was performed to evaluate light absorption behavior and electronic transition characteristics of synthesized nanoparticles. The diffuse reflectance spectrum, shown in Fig. 4(a), exhibits strong absorption throughout the UV–visible region, indicating the excellent visible-light harvesting capability of the tulsi-assisted ZCCO nanoparticles. Such optical behavior suggests that the synthesized material is a promising candidate for photocatalytic applications under visible-light irradiation. In previous reports, UV–DRS analysis revealed changes in optical absorption and band-gap energy on green-synthesized CeO_2 nanoparticles. These variations were attributed to phytochemical-mediated modifications in the electronic structure of the metal oxide lattice, thereby influencing its optoelectronic behavior (Baitha *et al.* 2026).

Optical band-gap energy of tulsi-derived ZCCO nanoparticles was estimated using the Kubelka–Munk approach, as illustrated in Fig. 4(b). This method establishes a relationship between absorption coefficient (K), diffuse reflectance (R), and scattering coefficient (S) of synthesized nanoparticles. The Kubelka–Munk function was employed to evaluate optical transition behavior and determine band-gap energy of ZCCO photocatalysts from the diffuse reflectance data.

$$F(R) = \frac{(1-R)^n}{2R} = \frac{K}{S} \qquad \ldots (3)$$

The parameter n represents nature of electronic transition, where $n = 1/2$ corresponds to allowed transition and $n = 2$ indicates indirect allowed transition. Optical band-gap energy and absorption characteristics of synthesized ZCCO nanoparticles were estimated using Tauc equation, which relates absorption coefficient (α) to incident photon energy

$$a = \frac{C_1(hv-Eg)^{\frac{1}{2}}}{hv} \qquad \ldots (4)$$

$$[F(R)hv]^2 = C_2[hv - Eg] \qquad \ldots (5)$$

Optical band-gap energy of tulsi-assisted ZCCO nanoparticles was obtained using extrapolating linear portion of $[F(R)hv]^2$ *vs* hv plot to energy axis at $[F(R)hv]^2 = 0$. Estimated band-gap value of

synthesized ZCCO nanoparticles was found to be approximately 2.45 eV, as illustrated in Fig. 4(b).

3.4 Photocatalytic Studies

Photocatalytic dye degradation studies were carried out in cylindrical glass reactor. Dyes used were fast orange and Fast Blue (FB). Suspension was irradiated using a 125 W mercury vapor lamp positioned 25 cm from the reactor. Approximately 60 mg of tulsi-mediated ZCCO nanoparticles were dispersed at 250 mL of dye solution with initial concentration of 20 ppm. Throughout the experiment, suspension was continuously stirred by magnetic stirrer to maintain dispersion of the photocatalyst particles. The adsorption capacity (Q) of synthesized ZCCO nanoparticles were calculated using following equation.

$$Q = \frac{(C_O - C)}{W} \quad \ldots (6)$$

The photocatalytic performance of the tulsi-derived ZCCO nanoparticles is presented in Fig. 5(a–c), based on degradation of FO and FB dye solutions at UV irradiation. The synthesized ZCCO nanoparticles exhibited excellent photocatalytic efficiency, which can be attributed to effective charge separation and enhanced reactive species during irradiation. The degradation efficiency toward FB reached approximately 90.5% after 120 minutes of UV irradiation. In contrast, FO exhibited superior degradation behavior, achieving approximately 92.8% discoloration within the same irradiation period, as shown in Fig. 5(c). At predetermined intervals (0–120 minutes), aliquots from the 250 mL dye suspension were collected, centrifuged, and analyzed using UV–Visible spectroscopy. The degradation process was monitored at the characteristic absorption wavelengths of approximately 604 nm for FO and 597 nm for FB.

Fig. 5(d) illustrates the variation of $\log(C/C_0)$ during photocatalytic degradation of FO and FB dyes at UV irradiation in the presence of tulsi-mediated ZCCO nanoparticles. The $\log(C/C_0)$ values were calculated to evaluate degradation kinetics and photocatalytic efficiency of synthesized nanoparticles.

$$\log(C/C_O) = -\mathrm{kt} \quad \ldots (7)$$

The higher rate constant obtained for FO indicates a faster degradation process compared with FB under identical experimental conditions. Furthermore, the percentage photocatalytic degradation of the FO and FB dye solutions was calculated using the following expression:

$$\%D = \frac{C_O - C}{C_O} \times 100 \quad \ldots (8)$$

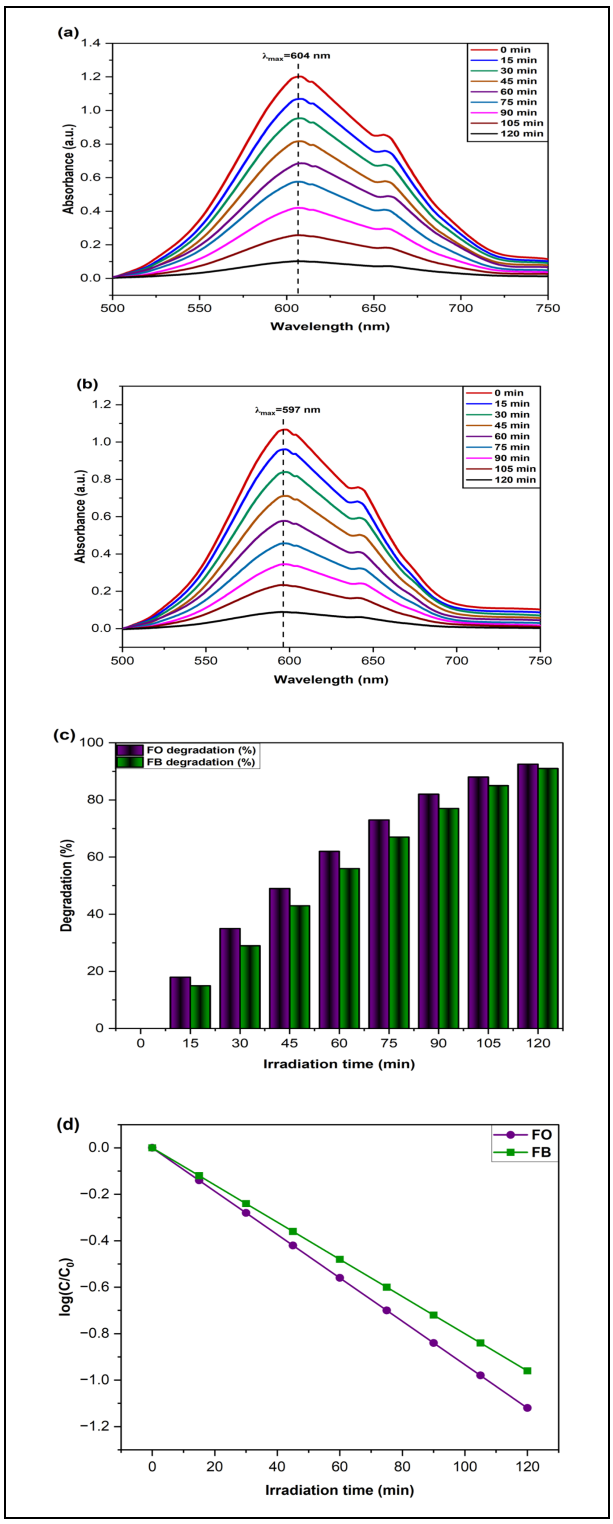

Fig. 5: (a,b) UV–Vis absorption spectra of fast orange and fast blue during photocatalytic degradation under UV irradiation. (c) Photodegradation efficiency of FO and FB dyes and (d) First-order kinetic plots for FO and FB degradation using ZCCO nanoparticles

In this equation, C_o shows initial concentration of dye solution, while C shows remaining dye concentration after photocatalytic treatment. The term *%D* corresponds to the percentage degradation (decolorization) efficiency, which reflects the ability of tulsi-mediated ZCCO nanoparticles to remove dye molecules from the aqueous medium under irradiation. According to previous studies, green-synthesized MgO nanoparticles achieved photocatalytic degradation efficiencies of 80.35% for FO and 80.50% for FB dyes under UV irradiation, demonstrating effective photocatalytic activity (Asha *et al.* 2025).

3.5 Photocatalytic Degradation Mechanism of ZCCO Nanoparticles Under UV Irradiation

The photocatalytic reaction mechanism illustrates the interaction between dye molecules and the reactive species generated on the surface of tulsi-mediated ZCCO nanoparticles under light irradiation. The sequential process demonstrates the efficient generation of reactive oxygen species, leading to the degradation of dye molecules and highlighting the potential of the synthesized ZCCO nanoparticles for wastewater treatment applications.

The following mechanism explains the overall photocatalytic degradation of FO and FB dyes by ZCCO nanoparticles.

Absorption of UV light by ZCCO:

$$\mathrm{ZCCO} + h\nu \rightarrow e^- + h^+ \quad \ldots (9)$$

Formation of hydroxyl radicals from water molecules:

$$h^+ + H_2O \rightarrow \cdot OH + H^+ \quad \ldots (10)$$

Reduction of dissolved oxygen to superoxide radicals:

$$O_2 + e^- \rightarrow O_2^- \quad \ldots (11)$$

Conversion of superoxide radicals into hydroperoxyl radicals:

$$O_2^{--} + H^+ \rightarrow \cdot OOH \quad \ldots (12)$$

Formation of hydrogen peroxide through radical reactions:

$$O_2^{--} + 2H^+ + e^- \rightarrow H_2O_2 \quad \ldots (13)$$

Generation of additional hydroxyl radicals from hydrogen peroxide:

$$H_2O_2 + e^- \rightarrow \cdot OH + OH^- \quad \ldots (14)$$

Oxidative degradation of dye molecules:

$$\text{Dyes} + (\cdot OH + O_2^- + \cdot OOH) \rightarrow \text{Degradation products} \quad \ldots (15)$$

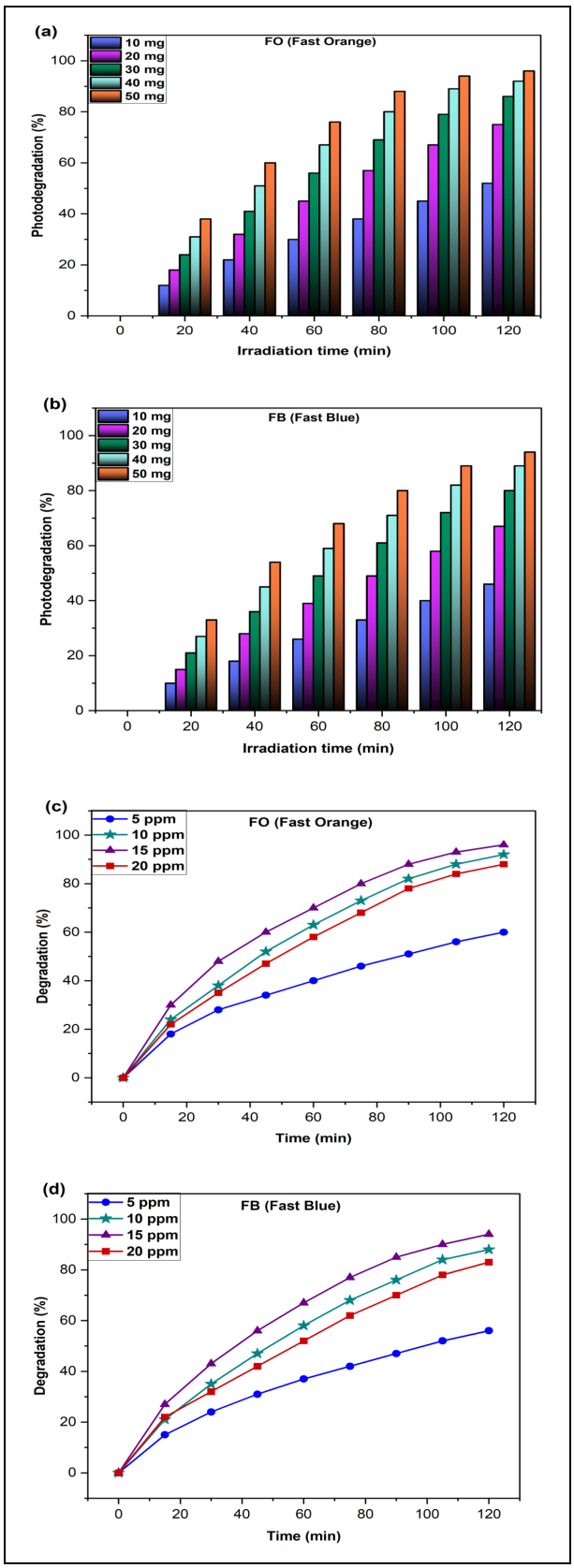

Fig. 6: (a,b) Photocatalyst dosage on photocatalytic degradation of FO and FB dyes, (c,d) Initial dye concentration on degradation of FO and FB dyes using ZCCO nanoparticles

This mechanism describes the photocatalytic decolorization of FO and FB dyes by the synthesized tulsi-mediated ZCCO nanoparticles.

Reusability studies of the ZCCO photocatalyst were performed under optimized experimental conditions. After all degradation cycles, nanoparticles were recovered by filtration, washed thoroughly, and dried for subsequent use. A slight reduction at degradation efficiency were observed after first cycle; however, the performance remained nearly unchanged up to the fifth cycle.

As shown in Fig. 6(a,b), the photocatalytic degradation increased with increasing catalyst dosage. Photocatalytic degradation efficiency of FO and FB dyes was strongly dependent on the amount of tulsi-mediated ZCCO photocatalyst employed. The highest value at 15 ppm achieved approximately 96% degradation for FO and 94% for FB after 120 minutes of UV irradiation. A slight decrease in degradation efficiency was observed at 20 ppm, which can be attributed to increased shielding effects, reduced photon penetration, and competition among dye molecules for the available active sites on the photocatalyst surface as shown in Fig. 6(c, d).

Radical scavenging experiments were performed to check the involvement of reactive species during photocatalytic degradation process. Both, FO and FB dye solutions were irradiated under UV light in the presence of ZCCO nanoparticles and different scavengers. The degradation efficiencies obtained using ethanol, $AgNO_3$ and benzoic acid were 89.14%, 82.06% and 80.25% for FO, and 78.42%, 74.15% and 67.31% for FB, respectively. The results indicate that $\cdot OH$ radicals and photogenerated holes played dominant roles in dedegradation, whereas O_2^{--}contributed comparatively less. Accordingly, contribution of reactive species was $\cdot OH > h^+ > O_2^{--}$.

The influence of H_2O_2 on photocatalytic performance was also investigated as it can enhance generation of reactive oxidative species. Fig. 7 (a,b) present the effect of H_2O_2 addition on dye degradation using ZCCO nanoparticles (20 ppm dye concentration and 20 mg catalyst dosage). In the absence of H_2O_2, the degradation efficiencies of FO and FB were 94% and 82%, respectively. Upon the addition of 0.5 mM H_2O_2 under UV irradiation, the degradation efficiency increased from 94% to 98% for FO and from 82 to 95% for FB. In previous studies, the enhanced photocatalytic performance was attributed to improved charge separation and increased active surface sites. Similar results were reported for $CoCuFe_2O_4$-based GO/ZnS nanocomposites, achieving 99.9% methylene blue and 99.6% rhodamine B degradation under light irradiation (Sarker *et al.* 2026).

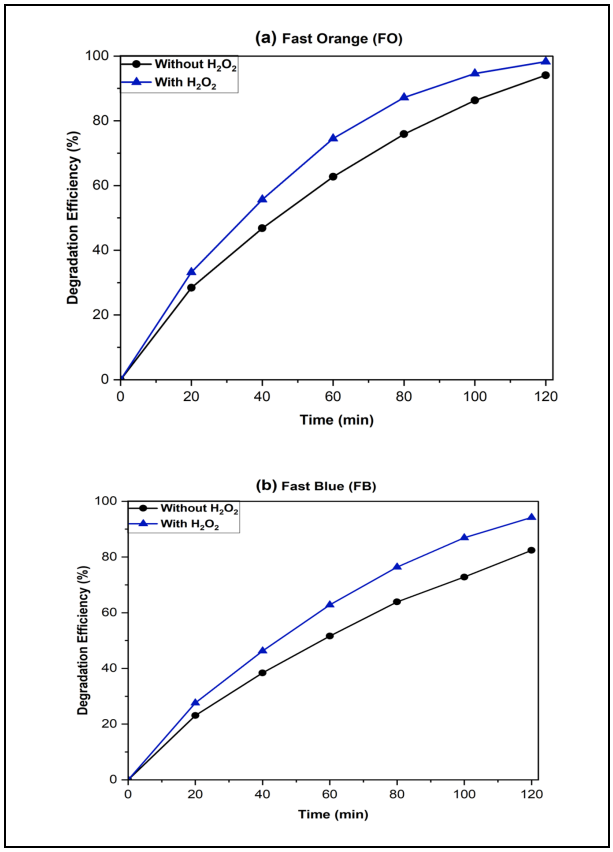

Fig. 7: Effect of H_2O_2 on photocatalytic degradation of (a) FO and (b) FB dyes using ZCCO nanoparticles under UV irradiation

3.6 Electrochemical Activity

Fig. 8(a) presents the cyclic voltammetry profiles of the tulsi-mediated ZCCO nanoparticles. The obtained CV curves deviated from ideal rectangular shape associated by electric double-layer capacitors, indicating the contribution of faradaic charge-storage processes. Observed capacitance behavior was attributed to reversible redox occurring at electrode–electrolyte interface. Potential difference among reduction peak potential (E_r) and oxidation peak potential (E_o) is an important parameter for evaluating electrode reversibility; lower values correspond to better reversibility. As shown in the figure, the ZCCO electrode exhibited pronounced redox characteristics with E_o–E_r values of 0.24 V and −0.18 V, corresponding to a peak separation (ΔE_p) of approximately 0.42 V. These results show that green-synthesized ZCCO nanoparticles possess favorable electrochemical behavior and enhanced charge-storage capability. Similarly, in previous studies tulsi-assisted green synthesized Zn-doped CeO_2 nanoparticles showed improved crystallinity, tunable optical characteristics, and enhanced electrochemical performance. The synthesized nanomaterials exhibited promising charge storage capability, demonstrating their potential for advanced energy storage applications (Munirathnam *et al.* 2023).

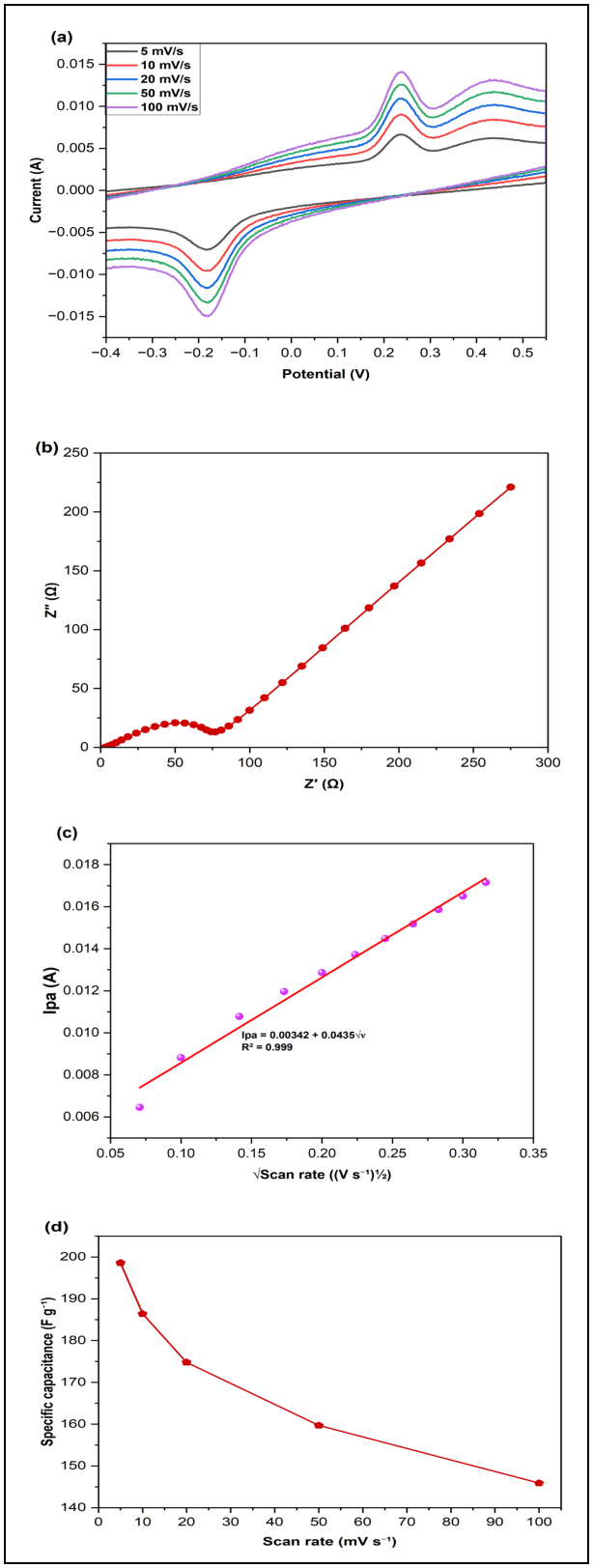

Fig. 8: (a) Cyclic voltammograms at different scan rates, (b) Nyquist impedance plot, (c) Anodic peak current vs square root of scan rate (v½) for ZCCO NPs and (d) Specific capacitance as a function of scan rate for the ZCCO electrode

Electrochemical results revealed good charge-transfer characteristics and satisfactory electrode reversibility. The specific capacitance (C_s) of the tulsi-mediated ZCCO electrode was:

$$C_s = \frac{A}{2mvdv} \quad \ldots (16)$$

Furthermore, peak current response for reversible redox process was described using Randles–Sevcik equation:

$$i_p = 2.69 \times 10^5 \times n^{3/2} \times A \times D^{1/2} \times C_O \times v^{1/2} \ldots (17),$$

where (n) is number of electrons involved in reaction, (i_p) is peak current (A), (D) is diffusion coefficient (cm² s⁻¹), (A) is electrode surface area (cm²), (n^3) is scan rate (Vs⁻¹), and (C_O) is concentration of electroactive species (mol cm⁻³).

$$C_O = \frac{\rho}{M} \quad \ldots (18)$$

Here, (M) denotes the molar mass and ρ represents the theoretical density of ZCCO.

Fig. 8(b) presents Nyquist plots of ZCCO electrode. The impedance spectra provide information regarding charge-transfer behavior and interfacial resistance of electrode material. In high-frequency region, plots exhibited depressed semicircular arcs with centers located below the real axis, indicating non-ideal capacitive behavior.

Linear dependence indicates that electrochemical response of the ZCCO electrode is predominantly controlled by a diffusion-assisted charge-transfer process. Using Equations (17) and (18), the diffusion coefficient ((D)) of ZCCO electrode was estimated from slope of fitted line in and was found to be 6.4×10^{-5} cm² s⁻¹. Relationship among square root of scan rate and cathodic peak current is shown in Fig. 8(c).

Constant phase element (CPE) (Q1) was incorporated into equivalent circuit model, where Q1 is expressed as:

$$Z_{CPE} \text{ or } Q1 = \frac{1}{Y(j\omega)^n} \quad \ldots (19),$$

where (Y) and (n) are the fitting parameters of CPE, and ω represents the angular frequency (rads⁻¹). The value of (n) approaches 1 for an ideal capacitor, 0 for a pure resistor, and 0.5 for a Warburg diffusion element. In Nyquist plot, intercept at high-frequency region to solution resistance (R_s), inclined line observed at low frequencies was associated with Warburg diffusion component ((W)).

A reduction in R_{ct} to 72 Ω together with an increase in double-layer capacitance Cdl to 1.86×10^{-4} F

indicates enhanced electrochemical performance of the tulsi-mediated ZCCO electrode, as shown in Fig. 8(d).

Galvanostatic charge–discharge of ZCCO electrode recorded at various current densities are presented in Fig. 9(a).

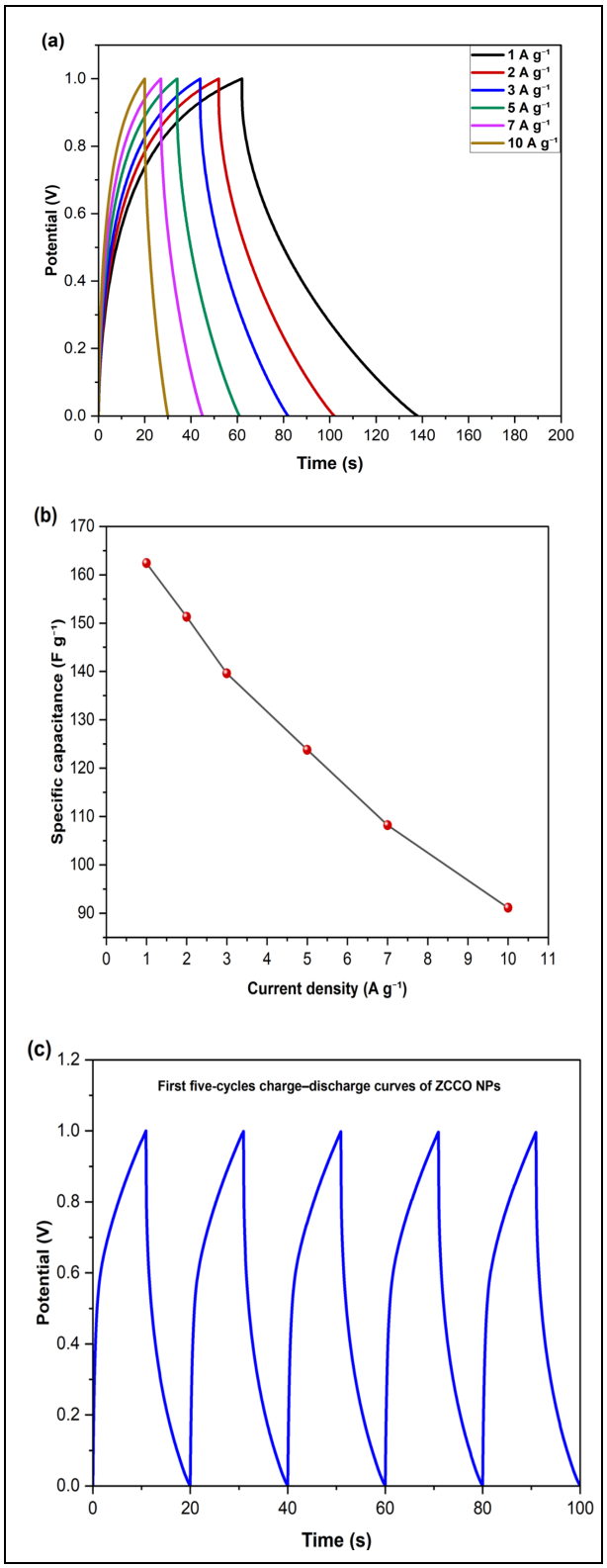

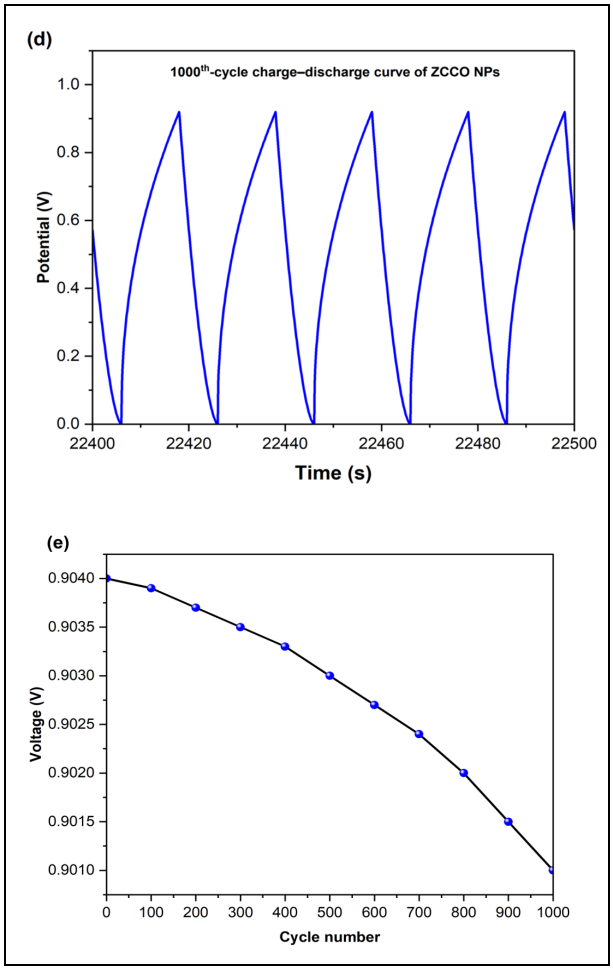

Fig. 9: (a) Galvanostatic charge–discharge curves at different current densities (b) Specific capacitance as a function of current density (c) Initial five-cycle galvanostatic charge–discharge profiles (d) 1000th-cycle galvanostatic charge–discharge profile of the ZCCO electrode and (e) Voltage profile versus cycle number for ZCCO NPs

As evident from Fig. 9(b), charge–discharge profiles exhibit characteristics typical of pseudocapacitive materials rather than ideal electric double-layer capacitors, which are consistent with CV outcomes. The non-linear nature of curves confirms contribution of faradaic redox reactions to overall charge-storage process. Generally, increase at current density resulted in enhanced charge–discharge behavior and improved rate capability. Specific capacitance of tulsi-mediated ZCCO electrode was calculated using following equation.

$$C = \frac{i\Delta t}{m\Delta V} \quad \ldots (20),$$

where (t) is discharge time, (i) is applied current, ΔV is potential window and (m) is mass of active ZCCO material. Specific capacitance calculated using equation (20) confirmed the good charge-storage capability of tulsi-mediated ZCCO electrode. The maximum specific

capacitance, energy density, and power density was found to be 162.3 F g^{-1}, 22.5 Wh kg^{-1}, and 500 W kg^{-1}, respectively.

Galvanostatic charge–discharge profiles of ZCCO electrode recorded at various current densities are presented in Fig. 9(c). Shape of charge–discharge curves further confirms the pseudocapacitive behavior observed in cyclic voltammetry measurements. An increase in current density generally resulted in improved rate performance. Long-term cycling was assessed through galvanostatic charge–discharge testing at 1 A g^{-1} for 1000 cycles, and results are shown in Fig. 9(d). Fig. 9(e) shows the voltage profile *versus* cycle number for ZCCO NPs. Previously a study reported enhanced electrochemical activity for CeO_2-integrated bimetallic sulfide electrodes, with $ZnCoS/CeO_2$ delivering a specific capacitance of 616.25 F g^{-1} at 1 A g^{-1} and 86.7% capacitance 2500 cycles (Maghool *et al.* 2026).

4. CONCLUSIONS

Tulsi (*Ocimum tenuiflorum*) leaf extract and a green combustion approach were employed for synthesis of Zinc-Copper-Cobalt Oxide nanoparticles. The synthesized ZCCO nanoparticles exhibited good crystallinity with an average crystallite size of 19.8 nm. The PXRD analysis confirmed successful formation of a crystalline mixed-metal oxide phase. The SEM observations revealed a relatively uniform, porous, and less agglomerated morphology. Optical band-gap energy of ZCCO nanoparticles was determined to be 2.45 eV. Photocatalytic studies showed excellent degradation performance toward FB and FO dyes under UV irradiation, achieving degradation efficiencies of 92.8% and 90.5%, respectively, after 120 minutes. Effect of catalyst loading was investigated by different ZCCO dosages from 10 to 50 mg maintaining dye concentration at 20 ppm, and maximum degradation efficiency was obtained at 50 mg.

Scavenger experiments by ethanol, $AgNO_3$, and benzoic acid revealed degradation efficiencies of 89.14%, 82.06%, and 80.25% for FO, and 78.42%, 74.15%, and 67.31% for FB, respectively, confirming involvement of reactive species at degradation process. Cyclic voltammetry studies performed using ZCCO-coated nickel mesh electrodes in 1 M KOH electrolyte demonstrated distinct redox behavior and favorable charge-storage characteristics. Electrochemical impedance spectroscopy indicated improved electrochemical activity due to reduced charge-transfer resistance. The diffusion coefficient of ZCCO electrode was estimated to be 6.4×10^{-5} cm^2 s^{-1}. The galvanostatic–discharge analysis yielded specific capacitance of 162.3 F g^{-1}. Cycling stability tests conducted at 1 A g^{-1} for 1000 cycles charge–discharge profile demonstrated excellent electrochemical stability. The outcomes demonstrate that synthesized ZCCO nanoparticles are promising materials for photocatalytic wastewater treatment and electrochemical energy applications.

FUNDING

This research received no specific grant from any funding agency in the public, commercial, or not-for-profit sectors.

CONFLICTS OF INTEREST

The authors declare that there is no conflict of interest.

COPYRIGHT

This article is an open-access article distributed under the terms and conditions of the Creative Commons Attribution (CC BY) license (http://creativecommons.org/licenses/by/4.0/).

REFERENCES

Adarshgowda, N., Naik, H. S. B., Vishnu, G., Manjunatha, K. G. and Hareeshanaik, S., Impact of green-synthesized Mg-doped Mn ferrite nanoparticles on light-driven degradation of dyes and their optoelectronic applications, *New J. Chem.*, 48(29), 13155–13170(2024). https://doi.org/10.1039/d4nj02377c

Allah, S. M., Aslam, M. K., Hameed, S., -ul-Haq, M. E., Hussain, S., Al-Marzouqi, A. H. and Xu, M., Hierarchical sea-urchin anchored on rGO sheets decorated with layered double hydroxide nanoflowers: A novel electrode for enhanced supercapacitor performance, *J. Energy Storage*, 172, 122965 (2026). https://doi.org/10.1016/j.est.2026.122965

Ansari, Z., Kadam, S., Kasabe, S., Tripathi, J., Agale, P., Patange, S. and More, P., Optimized Mn doped ZnO@rGO nanocomposites: a breakthrough for advanced energy storage and PEC systems, *Ionics*, 31(8), 8151–8172 (2025). https://doi.org/10.1007/s11581-025-06468-x

Arpitha, S. B., Kumara Swamy, B. E. and Shashikumara, J. K. An efficient electrochemical sensor based on ZnO/Co_3O_4 nanocomposite modified carbon paste electrode for the sensitive detection of hydroquinone and resorcinol, *Inorg. Chem. Commun.*, 152, 110656 (2023). https://doi.org/10.1016/j.inoche.2023.110656

Asha, S. C., Divakara, S. G., Mahesh, B., Ravikumar, C. R. and Murthy, H. C. A., Improved photocatalytic activity triggered by UV light, as well as electrochemical sensing characteristics of MgO nanoparticles, *Int. J. Environ. Anal. Chem.*, 105(18), 6221–6240 (2025). https://doi.org/10.1080/03067319.2024.2415528

Baitha, R., Das, A. K., Kumar, S. and Manash, A., Green vs. chemical cerium oxide nanoparticles (CeO_2-NPs): Integrated assessment of synthesis pathways, structural properties, ferroelectric behavior, and biomedical applications, *Solid State Commun.*, 409, 116309 (2026). https://doi.org/10.1016/j.ssc.2025.116309

Gaikwad, P. G., Mahamuni, G. P., Naik, N., Kulkarni, S. B. and Hiremath, P., Substrate driven growth of quaternary CoNiCuZn oxide nanostructures via electrodeposition for enhanced supercapacitor applications, *Discover Mater.*, 6(1), 13(2026). https://doi.org/10.1007/s43939-025-00439-9

Gunasekaran, Y., Suntharam, N. M., Bashir, S., Vengadaesvaran, B., Gunasegeran, S., Gopalakrishnan, N., Ramesh, S., Ramesh, K., Gerard, O. and Pershaanaa, M., Synthesis and characterization of ZnO/biochar composite as electrode material for hybrid supercapacitor, *Ionics*, 32(2), 1987-2010(2025). https://doi.org/10.1007/s11581-025-06839-4

Jose, V., Jose, V., Kuruvilla, E., Arunkumar, M., Deepi, A. S., Srikesh, G. and Nesaraj, A. S., Facile chemical synthesis of mixed Zn-Co manganite based tetragonal spinels for energy storage and environmental remediation, *Optik*, 291, 171335(2023). https://doi.org/10.1016/j.ijleo.2023.171335

Kavica, S., Rajesh, P., Velmani, V. and Parethe, G. T., Biological Synthesis of Cobalt Oxide Nanoparticles Using Ziziphus oenopolia Leaf Extract, *J. Environ. Nanotechnol.,* 13(1), 85-91(2024). https://doi.org/10.13074/jent.2024.03.241510

Khawale, V. R., Kumar, R., Satishkumar, P., Haldar, B., Deepa, B., Saminathan, R., Veeramanikandan, P., Packirisamy, A. S. B. and Selvaraju, M., Study on Electrochemical Stability and Charge Transfer Efficiency for the Development of High-Performance Supercapacitors Using Iron Oxide (Fe_2O_3) Nanorods, *J. New Mater. Electrochem. Syst.*, 27(3), 163–171(2024). https://doi.org/10.14447/jnmes.v27i3.a01

Kubendhiran, S., Chung, R. J., Kongvarhodom, C., Chen, H. M., Yougbaré, S., Saukani, M., Wu, Y. F. and Lin, L. Y., Fast Fabrication of High-Performance Supercapacitor Electrodes Based on Two-Dimensional Trimetallic Zinc Manganese Cobalt-Layered Double Hydroxide Nanosheets Derived from Metal-Organic Frameworks, *ACS Appl. Energy Mater.*, 8(10), 6339–6352 (2025). https://doi.org/10.1021/acsaem.5c00018

Kumari, T., Phogat, D. and Shukla, V., Exploring the multipotentiality of plant extracts for the green synthesis of iron nanoparticles: A study of adsorption capacity and dye degradation efficiency, *Environ. Res.*, 229, 116025(2023). https://doi.org/10.1016/j.envres.2023.116025

Maghool, S., Asgharinezhad, A. A., Molaei, Z., Larimi, A. and Gotbi, C., CeO_2-modified bimetallic sulfides for efficient energy storage in supercapacitors: A comparative study of ZnCoS and CuCoS, *Mater. Today Chem.*, 54, 103684(2026). https://doi.org/10.1016/j.mtchem.2026.103684

Marchetti, D., Scaravonati, S., Anyfanti, G., Aversa, L., Verucchi, R., Riccò, M., Massera, C., Gemmi, M., Pontiroli, D. and Pedrini, A., A green and efficient strategy for fabricating supercapacitor electrodes using a mechanochemically synthesised Cu-HHTP MOF, *J. Mater. Chem. A*, 14(27), 17207–17217(2026). https://doi.org/10.1039/d6ta00182c

Maskaric, K., Ammar, A. U., Nan, A., Radu, T., Rostas, A. M. and Terenti, N., Transition metal-complexed lactone-functionalized poly(benzofuran-co-arylacetic acid) for enhanced supercapacitor efficiency, *J. Energy Storage*, 159, 121897(2026). https://doi.org/10.1016/j.est.2026.121897

Moroz, M., Tesfaye, F., Demchenko, P., Prokhorenko, M., Rudyk, B., Pereviznyk, O., Mastronardo, E., Lindberg, D., Reshetnyak, O. and Hupa, L., Phase Equilibria and Thermodynamic Properties of Selected Compounds in the Ag–Ga–S–AgBr System for Modern Application in Energy Conversion Devices, *Minerals, Met. Mater. Series*, 257–268 (2024). https://doi.org/10.1007/978-3-031-50244-6_23

Munirathnam, R., Farheen, S. M. R., Manjunatha, S., Manjunatha, H. C., Vidya, Y. S., Sridhar, K. N., Seenappa, L., Veera, R. M. S. And Krishnaveni, S., Tulsi mediated green synthesis of zinc doped CeO_2 for super capacitor and display applications, *J. Sci. Adv. Mater. Dev.*, 8(2), 100551 (2023). https://doi.org/10.1016/j.jsamd.2023.100551

Nandagudi, A., Nagarajarao, S. H., Santosh, M. S., Basavaraja, B. M., Malode, S. J., Mascarenhas, R. J. and Shetti, N. P., Hydrothermal synthesis of transition metal oxides, transition metal oxide/carbonaceous material nanocomposites for supercapacitor applications, *Mater. Today Sustain.*, 19, 100214(2022). https://doi.org/10.1016/j.mtsust.2022.100214

Nazari, N., Mirzaee, S., Malek Khachatourian, A., Golmohammad, M., Javanmard, A., Sarraf-Mamoory, R., Zahrhuber, R. and Unterweger, C., Synthesis of CuO-ZnO/N, P-doped 3D rGO hybrid supercapacitive electrode: Fabrication and electrochemical characterization, *Solid State Sci.*, 173, 108186(2026). https://doi.org/10.1016/j.solidstatesciences.2025.108186

Panchal, P., Rauwel, P., Sharma, S., Nehra, S. P., Estephan, E., Praakle, K. and Rauwel, E., Ocimum tenuiflorum leaf-mediated graphitic carbon nitride and ZnO/GCN nanohybrid: a sustainable approach for environmental applications, *Environ. Sci. Pollut. Res.*, 32(15), 9945–9965(2025). https://doi.org/10.1007/s11356-025-36299-2

Pandey, P., Joshi, C. S. and Choubey, A. K., Lemon juice assisted synthesis of ternary ZnO@CuO@PANI nanocomposite as an efficient dielectric material for high-frequency applications, *Polym. Bulletin*, 83(8), 429 (2026). https://doi.org/10.1007/s00289-026-06492-5

Pooja, K. R., Chikkatti, B. S., Sajjan, A. M., Manjanna, J. and Nagaraju, G., Engineering of β-$Cu_2V_2O_7$ nanostructures for bifuntional use in environmental monitoring and supercapacitor applications, *J. Ind. Chem. Soc.*, 102(10), 102040(2025). https://doi.org/10.1016/j.jics.2025.102040

Rahman, M. M., Alam, M. M. and Asiri, A. M., Highly sensitive sensor probe development with ZCCO nano-capsule composites for the selective detection of unsafe methanol chemical by electrochemical technique, *Appl. Nanosci.,* 12(5), 1571–1584(2022). https://doi.org/10.1007/s13204-022-02354-4

Revathi, M., Nithya, G., Gunasekaran, S. S., Dhanalakshmi, E., Rajesh, P. and Lee, C. W., One-Pot Dual-Phytochemical Synthesis of Nickel Oxide Nanoparticles from Eclipta prostrata and Ocimum tenuiflorum as a Green Electrode for High-Performance Pseudo-Capacitor, *JOM*, 78(2), 1623–1632 (2026). https://doi.org/10.1007/s11837-025-07939-2

Salamon, J., Simi, A., Prabu, H. J., Sahayaraj, A. F., Kennedy, A. J. S. and Johnson, I., Synthesis and Characterization of rGO-ZnO/Elwendia persica Seed Reinforced Hybrid Nanocomposite for High-Performance Supercapacitor Applications, *J. Inorg. Organomet. Polym. Mater.*, 35(1), 342–355(2025). https://doi.org/10.1007/s10904-024-03293-z

Sarker, M. I. R., Rahman, M. L., Hossain, M. J., Biswas, B., Ahmed, M. F., Jahan, S. A. and Sharmin, N., Multifunctional $CoCuFe_2O_4$ decorated GO & ZnS nanocomposites for halogen light & sunlight assisted photocatalytic degradation (Dye & Antibiotic) and humidity sensing: Microstructural, optical and electromagnetic properties, *Mater. Sci. Eng. B*, 326, 119168 (2026). https://doi.org/10.1016/j.mseb.2025.119168

Singh, A. K., Ocimum sanctum mediated phytosynthesis of metallic nanoparticles: A review, *Biores. Technol. Rep.*, 19, 101118(2022). https://doi.org/10.1016/j.biteb.2022.101118

Soundarraj, C., Sumathi, T., Sivakumar, G., Parkavi, S., Sridevi, O. A. and Guganathan, L., Enhanced supercapacitor and photocatalytic performance of Zn doped nickel molybdate nanoparticles, *Nanotechnol. Environ. Eng.*, 11(2), 63(2026). https://doi.org/10.1007/s41204-026-00539-8

Surya, R., Sakthinathan, S., Meenakshi, G. A., Arumugam, B., Venkatesh, K. and Chiu, T. W., Synthesis of a novel p-type delafossite $CuInO_2$ flowers anchored on Ti_3C_2 sheetsas a positive electrode for high performance asymmetric supercapacitor, *Ceram. Int.*, 51(16), 22810–22819(2025). https://doi.org/10.1016/j.ceramint.2025.01.562

Tian, F., Li, H., Wang, B., Cui, Y., Zheng, X., Wang, L., He, Z., Wang, S. and Liu, X., Co,N and Cu,N Co-doped ZnS with rich sulfur vacancies for high-performance supercapacitors, *J. Energy Storage*, 151, 120591 (2026). https://doi.org/10.1016/j.est.2026.120591

Viswanathan, A., Manohar, A. and Aravindan, V., High energy and durable PANI, CuO and ZnO nanocomposites for aqueous/organic supercapacitors and their H^+/NH^+4 ions co-intercalation, *Sci. Rep.*, 16(1), 15700(2026). https://doi.org/10.1038/s41598-026-45954-8

Vusenappagari, R. and Kumar, B. D., Green combustion synthesised Zn/NiO nanocomposite for photocatalytic and supercapacitor applications, *Int. J. Environ. Anal. Chem.*, 105(18), 7220–7239(2025). https://doi.org/10.1080/03067319.2024.2440807

Yadav, S., Kaur, R. and Singh, P., Biosynthesis of zinc-copper mixed metal oxide nanoparticles using button-lac extract: A novel approach to combat antimicrobial resistance, *Microbial Pathogenesis*, 215, 108482(2026). https://doi.org/10.1016/j.micpath.2026.108482